RSC Advances

ROYAL SOCIETY OF CHEMISTRY

www.rsc.org/advances

RSC Advances

ARTICLE

Enhanced Rate Capability of Lithium Ion Battery Anode Based on Liquid-Solid-Solution Assembly of Fe_2O_3 on Crumpled Graphene

Received 00th January 20xx,
Accepted 00th January 20xx

DOI: 10.1039/x0xx00000x

www.rsc.org/

Xinghong Cui,[a] Yanfang Zhu,[a] Fei Li,[c] Daijun Liu,[a] Jianjun Chen,[a] Yuxin Zhang,[c] Li Li Zhang,[b,*] and Junyi Ji[a,*]

We report a liquid-solid-solution assemble strategy to fabricate Fe_2O_3@graphene (Fe_2O_3@rGO) composites at the oil/water interface, where the Fe_2O_3 nanoplates with thickness of about 100 nm are anchored on the crumpled graphene sheets. The *in situ* nucleation and growth process can ensure intimate contact between Fe_2O_3 nanoplates and graphene sheets, while the oil shell on Fe_2O_3 can prevent the aggregation of the Fe_2O_3@rGO composite. The crumpled structure and the relatively thin Fe_2O_3 nanoplates can shorten the electron diffusion path and enhanced the utilization rate of the active material. When used as the anode material, the Fe_2O_3@rGO anode shows a high reversible capacity of 1160 mAh g^{-1} at 0.2 A g^{-1} after 100 cycles, as well as a high cycling stability (101.3% capacity retention after 300 cycles at 1 A g^{-1}). Moreover, with ~156 s charging time (at a current density of 12.8 A g^{-1}), the anode can deliver a significant capacity of 552 mAh g^{-1}, indicating its promising application as a high-rate lithium ion battery anode.

Introduction

Lithium ion batteries (LIBs) with high energy density, long lifespan and low cost are one of the most promising candidates for next-generation energy storage devices.[1-3] Si,[4,5] Co_3O_4,[6,7] Fe_2O_3,[8,9] NiO[10,11] *et al.* with high theoretical specific capacity have been widely investigated for high performance LIB anodes. Among them, Fe_2O_3 with high theoretical capacity (~1005 mAh g^{-1}), low cost, abundant and environmental benign in nature, has become a promising candidate for advanced electrode. However, the conductivity of the Fe_2O_3 monolith is limited, which lead to a poor rate performance at high current density. Meanwhile, the large volume expansion of Fe_2O_3 anodes during cycling can result in serious pulverization, which influence the irreversible capacity and cycle life.[12] Hence, development of Fe_2O_3-based anode materials with high capacity, rate capability and cycling stability is desired for next-generation electrodes.

Various strategies have proposed to avoid the pulverization and thereby enhance the structural stability and rate performance of the Fe_2O_3. One strategy is to construct nanosized architecture, such as nanorods,[13] nanofibers,[14] hollow-structures,[15] nanoplates,[16] which can shorten the diffusion paths of Li^+ and electrons, and release the strain caused by the volume change. Another one is to hybridize the nanosized active materials with conductive materials to enhance the conductivity of the composites, such as activated carbon,[17] carbon nanotube,[18] graphene,[19-21] conductive polymer[22] *et al.* Among them, graphene with high conductivity, two dimensional structure and good mechanical property, has become the first choice to fabricate advanced electrodes. Graphene sheets in the electrodes can not only facilitate the electron transfer to the active materials, the superior mechanical property and flexibility can also buffer the volume change of host material during discharge/charge process. Though the study of Fe_2O_3/graphene hybrids has made great progress,[9,23] anodes with high rate performance as well as high stability is still urgently demanded.

Here, we report a liquid-solid-solution assemble strategy to fabricate Fe_2O_3@graphene (short for Fe_2O_3@rGO) composite, where the Fe_2O_3 nanoplates with average diameter of about 500 nm in width and 100 nm in thickness are anchored on graphene sheets. The crumpled structure and the relatively thin Fe_2O_3 nanoplates can shorten the electron diffusion path and enhanced the utilization rate of the active material, while the intimate contact can facilitate the electron transfer from the conductive graphene sheets to Fe_2O_3. With such a structure, the Fe_2O_3@rGO anode shows a high reversible capacity of 1160 mAh g^{-1} at 0.2 A g^{-1} after 100 cycles, as well as a high cycling stability (101.3% capacity retention after 300 cycles at 1 A g^{-1}). With ~156 s charging time (at a current density of 12.8 A g^{-1}), the anode can deliver a significant capacity of 552 mAh g^{-1}, which is comparable to most of the

[a] College of Chemical Engineering, Sichuan University, Chengdu, Sichuan, 610065, China.
[b] Institute of Chemical and Engineering Sciences, A*STAR, 1 Pesek Road, Jurong Island 627833, Singapore.
[c] College of Material Science and Engineering, Chongqing University, Chongqing, 400044, China.
* Corresponding Author
Junyi Ji, E-mail: junyiji@scu.edu.cn
Li Li Zhang, Email: zhang_lili@ices.a-star.edu.sg
Electronic Supplementary Information (ESI) available: Additional characterization data of SEM images, electrochemical impedance spectroscopy (EIS) measurements are presented. See DOI: 10.1039/x0xx00000x

state-of-the-art anodes, indicating its promising application as a high-rate LIB anode.

Experimental Methods

Synthesis of Fe_2O_3@rGO composite.

Graphene oxide (GO) was synthesized from graphite by a modified Hummers' method. Fe_2O_3@rGO composite (Sample 7:3) was fabricated through a liquid-solid-solution (LSS) process. Briefly, $(NH_4)_2Fe(SO_4)_2{\cdot}6H_2O$ (0.24 g) was dissolved in GO aqueous solution (~1 mg mL^{-1}, 20 mL) to form a Fe^{2+} solusion under ultrasonic (Solution A, Fe_2O_3/GO experimental designed weight ratio of 7:3). Then, NaOH (1.50 g), DI water (10 mL), ethanol (20 mL) and oleic acid (10 mL) were mixed orderly under vigorous stir to form a clear solution (Solution B). After addition of solution A dropwise to solution B under vigorous stir, the color of the mixture changed from black-brown to black. After stir for another 30 min, the mixture was transferred into a 100 mL Teflon-lined stainless steel autoclave, and treated at 180 °C for 10 h. After cooling to room temperature naturally, the black precipitates were separated by centrifugation, washed with ethanol and DI water for several times, respectively. The product was obtained after frozen drying and thermal treatment at 500 °C for 4 h under N_2 atmosphere. For comparison, other composites (Fe_2O_3/GO experimental designed weight ratio of 5:5 and 9:1) were prepared using the same process with different Fe_2O_3/GO ratio as the contrast samples.

Structure characterization

X-ray powder diffraction (XRD) patterns were obtained by an X'Pert Pro MPD using a Cu Kα radiation. The morphology and structure were characterized by field-emission scanning microscope (SEM, JSM-5900LV) and high resolution transmission electron microscopy (HRTEM, FEI Tecnai G20). The actual content of the samples were determined by Q500 Thermogravimetric analyzer (TA instruments, USA) with a heating rate of 10 °C min^{-1} under air flow. X-ray photoelectron spectroscopy (XPS) analysis was performed using a PHI5000 Versa Probe. Raman measurements were carried out by HORIBA Jobin Yvon LabRAM HR with a 532 nm Nd-Yag laser.

Electrochemical characterization

Electrochemical experiments were performed using CR2032 coin-type cells. The working electrodes were prepared by mixing active material, acetylene black and poly(vinylidene fluoride) (8:1:1 in weight) in N-methyl pyrrolidone to form a slurry, then coated onto a copper disc and dried under vacuum at 120 °C for 12 h. The mass loading of each electrodes (including active materials and additives) was ~1 mg cm^{-2}. Pure Li foil and polypropylene membrane (Celgard 2400) was used as the counter electrode and the separator, respectively, and 1 M $LiPF_6$ in a mixture of ethylene carbonate and diethyl carbonate (1:1 by volume) was used as the electrolyte. Cell assembly was carried out in an Ar protected glovebox. The galvanostatic charge-discharge measurements (0.01-3 V) were performed on a LANHE (CT2001A) battery test system. Cyclic voltammetry (CV) was performed on a LK9805 electrochemical analyser under a scan rate of 0.1 mV s^{-1}. Electrochemical impedance spectroscopy (EIS) was carried out on a Zahner electrochemical workstation in a frequency range of 0.01-100 kHz with an amplitude of 10 mV. The specific capacity is calculated based upon the total active materials (Fe_2O_3 and rGO).

Results and discussion

The Fe_2O_3@rGO composite is fabricated through a novel liquid-solid-solution (LSS) process, where Fe_2O_3 nanoplates are formed at the oil/water (O/W) microemulsion interface on graphene (**Figure 1**).[24-27] Firstly, $(NH_4)_2Fe(SO_4)_2$ is dissolved in GO aqueous suspension, where Fe^{2+} ions can anchor on the oxygen-containing groups of GO sheets *via* electrostatic adsorption. Ethanol can act as the mutual solvent to bridge the water and oleic acid to form microemulsion with liquid phase (ethanol-oleic acid) and solution phase (ethanol-water). After that, NaOH can react with oleic acid to form sodium oleate, which has a hydrophilic head (sodium salt side) and a hydrophobic chain (carbon chain). After mixing these two solutions, an ion exchange process occurs between Na^+ and Fe^{2+}, and then ferrous oleate/GO complex is obtained. The hydrophobic chain of the ferrous oleates on GO sheets together with sodium oleates form a liquid (oil) phase shell outside the graphene sheets (the hydrophobic chain form the oil shell while the hydrophilic head is distributed on both side of the oil shell).[24] During hydrothermal treatment, the Fe^{2+} on GO sheets can act as the nucleus and grow on the GO sheets, while the phase transfer process can ensure plenty of Fe^{2+} ions delivered from aqueous solution to solid phase (GO sheet interface) by oleate. The *in situ* nucleation and growth process in LSS process can ensure intimate contact between Fe_2O_3 nanoplates and graphene sheets, while the oil shell on Fe_2O_3 nanoplates can prevent the aggregation of the Fe_2O_3@rGO composite. To the best of our knowledge, this LSS assembly process is the first time reported to fabricate the metal oxide/graphene composites.

The obtained composites before and after heat treatment are characterized by X-ray diffraction (XRD) to trace the crystal transition. **Figure 2a** shows all peaks of products are in good agreement with α-Fe_2O_3 (PDF #33-1346), α-FeOOH (PDF #29-

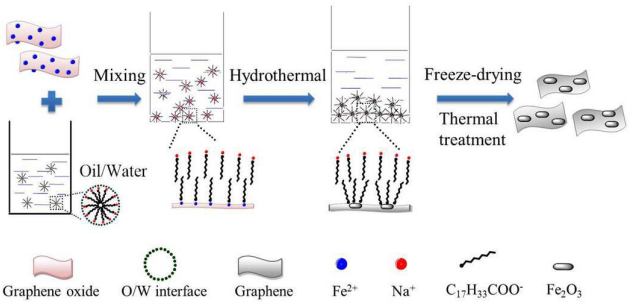

Figure 1. Illustration of the formation mechanism of Fe_2O_3@rGO composite

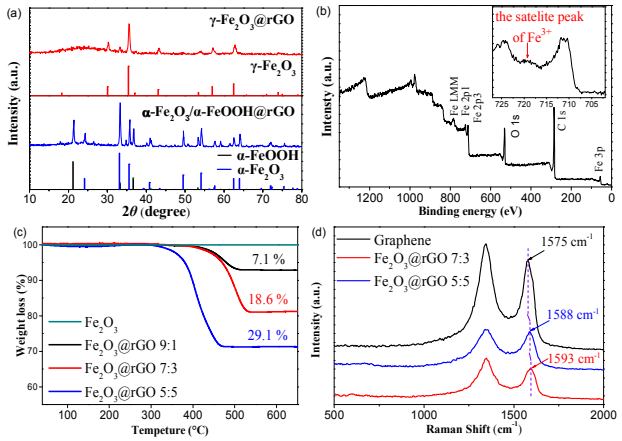

Figure 2. a) XRD patterns of Fe_2O_3/α-FeOOH@rGO and γ-Fe_2O_3@rGO. b) XPS spectrum of Fe_2O_3@rGO, inset is Fe 2p XPS spectrum of Fe_2O_3@rGO. c) TGA curves and d) Raman spectrums of Fe_2O_3@rGO with different Fe_2O_3 content.

2713) and γ-Fe_2O_3 (PDF #39-1346). This result reveals that the as-prepared composite is composed of hematite (α-Fe_2O_3) and goethite (α-FeOOH), while they are completely converted to γ-Fe_2O_3 during heat treatment *via* a dissolution-crystallization and dehydration-rearrangement process, respectively.[28] Furthermore, since the XRD patterns of Fe_3O_4 (PDF #19-0629) and the γ-Fe_2O_3 are similar, X-ray photoelectron spectroscopy (XPS) measurement has been carried out to verify the Fe^{2+} and Fe^{3+} cations (Figure 2b). The full spectrum indicates the presence of carbon, oxygen, and iron element, while the inset Fe 2p spectrum reveals two broad peaks and a satellite peak of Fe^{3+} around 710.9, 724.3 and 719.8 eV, respectively, all of which indicates the formation of γ-Fe_2O_3.[15] Thermogravimetric analysis (TGA) of Fe_2O_3@rGO (Figure 2c) reveals that the content of Fe_2O_3 in the composites are 70.9%, 81.4% and 92.9%, respectively (corresponds to Fe_2O_3@rGO (5:5), Fe_2O_3@rGO (7:3) and Fe_2O_3@rGO (9:1)), indicates the gradually increase of initial GO content can increase the mass content of rGO in the composites. The difference between the actual content and the experimentally designed value may be due to the deoxidization of GO sheets and the incomplete transfer of Fe ions. The Raman spectrums of Fe_2O_3@rGO (Figure 2d) reveals the G bands of the Fe_2O_3@rGO (5:5), Fe_2O_3@rGO (7:3) composite shift from 1575 cm^{-1} to 1588 cm^{-1} and 1593 cm^{-1}, respectively. The blue shift of the G band may introduced by the interaction between the graphene sheets and Fe_2O_3 nanoplates.[29]

Scanning electron microscopy (SEM) and high resolution transmission electron microscopy (HRTEM) are taken to investigate the morphology and structure evolution of the Fe_2O_3@rGO composites. **Figures 3a, b** present the structure of the composite before heat treatment (Fe_2O_3/FeOOH@rGO). The composite reveals a highly crumpled graphene sheet, and the Fe_2O_3/FeOOH nanoplates are uniformly anchored on graphene sheets without apparent aggregation, which may benefit by oil film protection during the LSS assembly. After heat treatment, the morphology of the obtained Fe_2O_3@rGO (7:3) composite does not change significantly (Figures 3c, d).

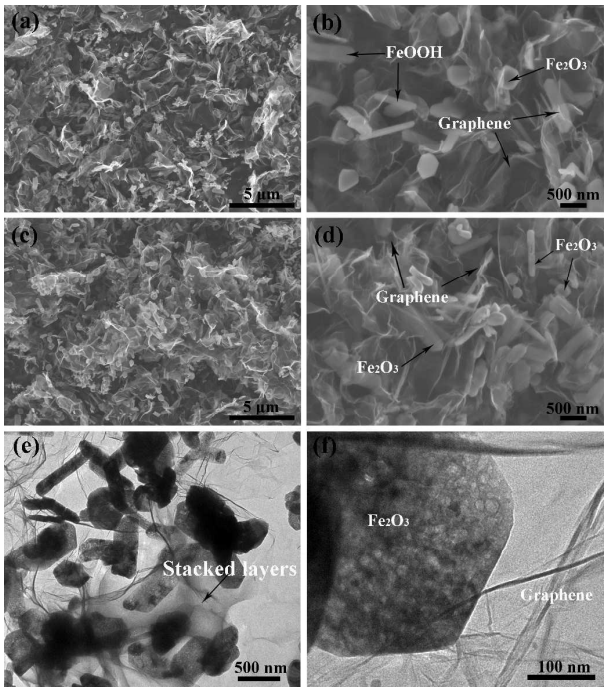

Figure 3. SEM images of a, b) Fe_2O_3/α-FeOOH@rGO (7:3) and c, d) Fe_2O_3@rGO (7:3) at different magnifications, and (e,f) TEM images of Fe_2O_3@rGO (7:3) at different magnifications.

Fe_2O_3 nanoplates uniformly anchored on crumpled graphene sheets are observed. The Fe_2O_3 nanoplates are about 500 nm in width and 100 nm in thickness (Figures 3e, f). Such thin nanoplates can shorten the electron diffusion path and enhanced the utilization rate of the active material. Furthermore, the composite structure can be retained after sonication, indicating good interaction between the graphene sheets and Fe_2O_3 nanoplates. On the contrary, the Fe_2O_3@rGO (5:5) composites show similar structure but with thicker graphene sheets, while the Fe_2O_3@rGO (9:1) shows highly aggregation of the Fe_2O_3 nanoplates on graphene sheets (**Figure S1**, see ESI). Moreover, the size of the Fe_2O_3 nanoplates show decrease trend with the decrease of the graphene content in the composites. This may be due to the different graphene content. The nucleus can be formed both on GO surface and in solution with insufficient GO sheets, which results in smaller Fe_2O_3 crystal size. The Fe_2O_3 nanoparticles suspended in solution trend to aggregation with Fe_2O_3@graphene composite to reduce the surface energy. In general, this crumpled Fe_2O_3@rGO composite may act as a high performance anode: the crumpled structure and the relatively thin Fe_2O_3 nanoplates can shorten the electrolyte ions diffusion pathway inside the electrode, while the intimate contact can facilitate the electron transfer rate from the conductive graphene sheets to active material (Fe_2O_3). Furthermore, the graphene sheets with high mechanical property can also buffer the stress from the volume expansion of the Fe_2O_3 nanoplates during cycling.

The electrochemical measurements of Fe_2O_3@rGO composites are firstly evaluated by cyclic voltammetry (CV). **Figure 4a**

RSC Advances

ARTICLE

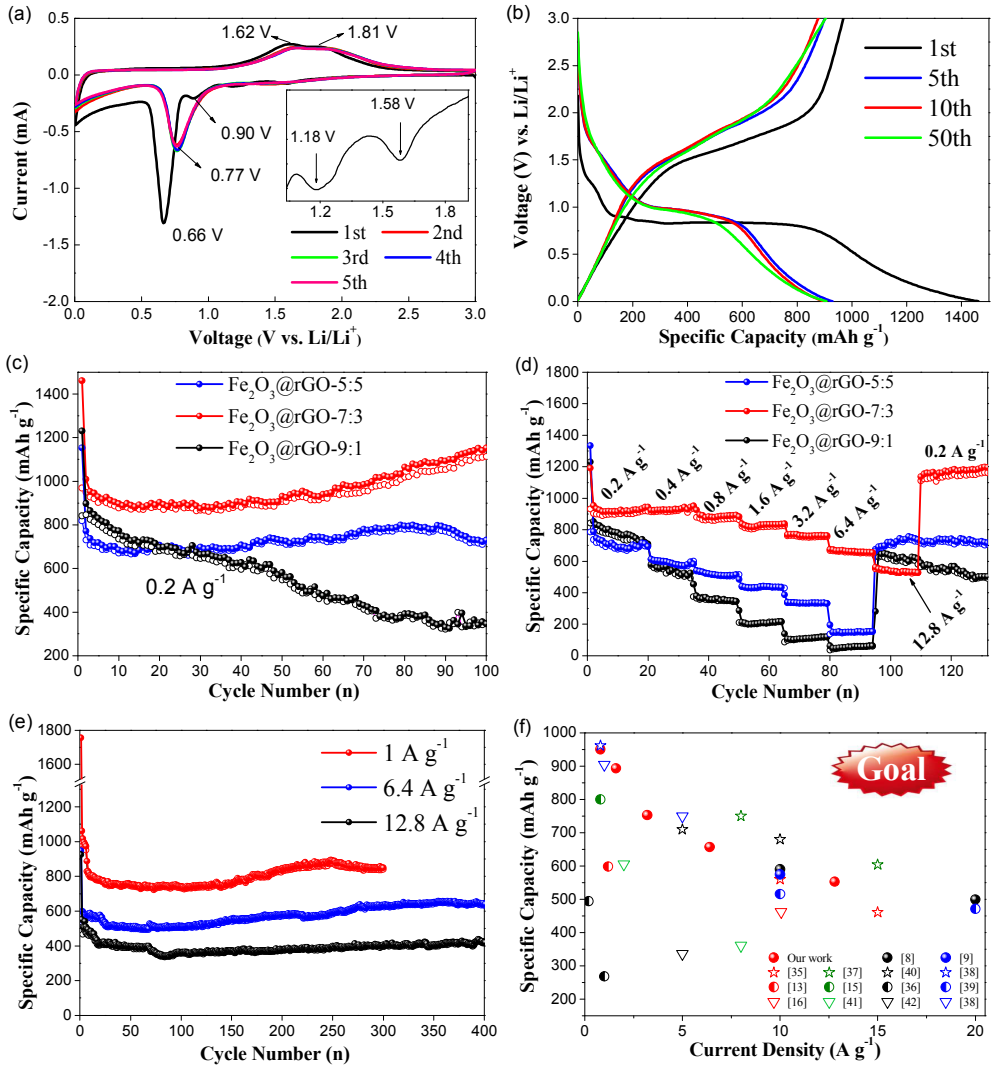

Figure 4. a) CV curves and b) galvanostatic charge/discharge profiles of Fe_2O_3@rGO (7:3) electrode at a scan rate of 0.1 mV s^{-1} and a current density of 0.2 A g^{-1}, respectively. c) Cycling performance of Fe_2O_3@rGO electrodes at a current density of 0.2 A g^{-1}, and d) rate performance of Fe_2O_3@rGO electrodes at different current densities with various graphene amount. e) Cycling performance of Fe_2O_3@rGO (7:3) at current density of 1, 6.4 and 12.8 A g^{-1}, respectively. f) Specific capacity at different current densities of the Fe_2O_3@rGO (7:3) electrode, comparing with some state-of-the-art LIBs anodes.

shows the CV curves of Fe_2O_3@rGO (7:3) electrode for the initial five cycles. During the first discharge cycle, the minor peaks at 1.58 and 1.18 V correspond to the initial lithiation reaction to form $Li_xFe_2O_3$.[16] The shoulder peak at 0.90 V is related to the phase change from hexagonal $Li_xFe_2O_3$ to cubic $Li_2Fe_2O_3$ for further Li-insertion.[16] The sharp peak at 0.66 V is caused by the reduction of Fe(III) to Fe(0) as well as the formation of solid electrolyte interface (SEI). During the charge cycle, the anodic peaks at 1.62 and 1.81 V are associated with the gradual oxidation of Fe(0) to FeO and then to Fe_2O_3.[12] In the following cycles, the center and the strength of the peaks remain the same, which reveals a high reversibility of the composite. This reversibility and stability can also be observed by the galvanostatic charge/discharge test. Figure 4b exhibits the charge/discharge curves of Fe_2O_3@rGO (7:3) at current density of 0.2 A g^{-1}. After the first cycle, the charge/discharge

curves of the 5th, 10th and 50th cycle show similar plateau voltage, as well as the specific capacity, indicating high stability and reversibility of the Fe_2O_3@rGO (7:3) electrodes.

The cycling and rate performance of the Fe_2O_3@rGO (7:3) electrodes are investigated. As shown in Figure 4c, an initial reversible specific capacity of 969 mAh g^{-1} is obtained, which is comparable to most of the iron-based electrodes.[14,30-33] After the slight decrease in the subsequent several cycles, the reversible specific capacity of Fe_2O_3@rGO (7:3) increases gradually, and reaches a high value of 1160 mAh g^{-1} after 100 cycles. This increase tendency and higher than theoretical specific capacity may be attributed to the gradual activation of Fe_2O_3, the synergistic effect of graphene and Fe_2O_3, as well as the pseudo-capacitive and the electron double layer capacitance (EDLC) of oxygen-containing graphene sheets.[16,20,30] Furthermore, the Fe_2O_3@rGO (7:3) electrodes exhibit a high rate performance, the specific capacity decreases slightly with the increase of current density (Figure 4d). The discharge capacities are 994.7, 950.3, 883.4, 837.2, 763.2 and 655.2 mAh g^{-1} at the current densities of 0.2, 0.4, 0.8, 1.6, 3.2 and 6.4 A g^{-1}, respectively. When the current density increases to as high as 12.8 A g^{-1} (corresponds to a charge time of 156 s), the specific capacity still reaches a high value of 552 mAh g^{-1}, indicating its potential as a high rate anode. Moreover, the reversible capacity can recover and keep the increase tendency once the current density is restored to 0.2 A g^{-1}, implying good reversibility of the anode.

In order to evaluate the cyclic stability under different charge rate, the Fe_2O_3@rGO (7:3) electrode tested under different current densities are also evaluated. The electrode show good long-term cycling stability (Figure 4e), at a current density of 1 A g^{-1}, the anode maintains a high capacity of 838.2 mAh g^{-1} (101.3% capacity retention) after 300 cycles with a Coulombic efficiency of almost 100%. When the current densities are up to 6.4 and 12.8 A g^{-1}, the discharge capacities are 636.4 and 419.8 mAh g^{-1} after 400 cycles and with a capacity retention of the about 107% and 81%, respectively, indicates the stable structure and high-rate performance of the Fe_2O_3@rGO 7:3 composite.

For comparison, the electrochemical performance of the Fe_2O_3@rGO (5:5) and Fe_2O_3@rGO (9:1) electrodes are also investigated (Figures 4c, d), both of them show inferior cycling and rate performance than the Fe_2O_3@rGO (7:3) electrode. The Fe_2O_3@rGO (5:5) electrode shows lower specific capacity value in cycling test and quick decrease during rate performance. The lower content of the active materials (Fe_2O_3), as well as the relatively larger Fe_2O_3 particle size and thicker graphene layer of the Fe_2O_3@rGO (5:5) electrode may hinder the electrolyte ions diffusion inside the electrode. On the other hand, the Fe_2O_3@rGO (9:1) composite show a high specific capacity in the beginning, then the values drop quickly in both the cycling and rate performance test. This may due to the lack of contact between graphene sheets and aggregated Fe_2O_3 nanoparticles, which can cause a high electron transfer resistance. To further understand the superior electrochemical performance of the Fe_2O_3@rGO (7:3) electrode, electrochemical impedance spectroscopy (EIS) measurements of these anodes are performed after 20 cycles activation. The Nyquist plots (**Figure S2**, see ESI) display that the diameter of the semicircle for Fe_2O_3@rGO (7:3) electrode in the high frequency region is smaller than the other two anodes, indicating lower ions and electrons diffusion resistance.[34] This result indicates that Fe_2O_3@rGO (7:3) electrode possesses the most balanced performance between the electron transfer and the electrolyte ions diffusion resistance, and explains its best electrochemical performance.

Besides the electrodes with different graphene content, some latest literature works on iron-based high-rate LIBs anodes are also taken into comparison. As shown in Figure 4f, the rate performance of the Fe_2O_3@rGO (7:3) electrode is comparable or higher than most of the state-of-the-art electrodes (including carbon-based anodes, and other metal oxide based anodes), especially under high current densities.[8,9,13-16,35-42] This improved rate performance of the Fe_2O_3@rGO (7:3) anode is attributed to its well designed structure: the electrical conductive graphene network and the good interaction between Fe_2O_3 and rGO ensures good electrical contacts and small charge transfer resistance; meanwhile, the graphene sheets can effectively relieve the stress of volume expansion upon material conversion process, reduces the pulverization and agglomeration of the electrode material. Considering the simple and scalable preparation method and low cost, this composite shows promise for application as high rate LIB anodes.

Conclusions

In summary, we fabricate Fe_2O_3 nanoplates anchored graphene composite with crumpled structure *via* a liquid-solid-solution assemble strategy. The crumpled structure as well as intimate contact between Fe_2O_3 nanoplates and graphene can facilitate the ions and electrons transfer inside the composite. The Fe_2O_3@rGO composites as anode shows a high reversible capacity of 1160 mAh g^{-1} at 0.2 A g^{-1} after 100 cycles, as well as a high cycling stability (101.3% capacity retention after 300 cycles at 1 A g^{-1}). With ~156 s charging time, the anode can deliver a significant capacity of 552 mAh g^{-1}, which is comparable to most of the high-end iron-based anodes, indicating its promising application as a high-rate LIB anode.

Acknowledgements

We appreciate the National Natural Science Foundation of China (21506130, 21490582).

References

1 B. Dunn, H. Kamath and J.-M. Tarascon, *Science*, 2011, **334**, 928-935.
2 M. Armand and J. M. Tarascon, *Nature*, 2008, **451**, 652-657.
3 J. Ji, Y. Li, W. Peng, G. Zhang, F. Zhang and X. Fan, *Adv. Mater.*, 2015, **27**, 5264-5279.
4 N. Liu, Z. Lu, J. Zhao, M. T. McDowell, H. W. Lee, W. Zhao and Y. Cui, *Nat. Nanotechnol.*, 2014, **9**, 187-192.

5 J. Ji, H. Ji, L. L. Zhang, X. Zhao, X. Bai, X. Fan, F. Zhang and R. S. Ruoff, *Adv. Mater.*, 2013, **25**, 4673-4677.
6 D. Wang, Y. Yu, H. He, J. Wang, W. Zhou and H. D. Abruña, *ACS Nano*, 2015, **9**, 1775-1781.
7 H. Hu, B. Guan, B. Xia and X. W. Lou, *J. Am. Chem. Soc.*, 2015, **137**, 5590-5595.
8 S. Chen, Y. Xin, Y. Zhou, F. Zhang, Y. Ma, H. Zhou and L. Qi, *J. Mater. Chem. A*, 2015, **3**, 13377-13383.
9 K. Cao, L. Jiao, H. Liu, Y. Liu, Y. Wang, Z. Guo and H. Yuan, *Adv. Energy Mater.*, 2015, **5**, 1401421.
10 J. Liang, H. Hu, H. Park, C. Xiao, S. Ding, U. Paik and X. W. D. Lou, *Energy Environ. Sci.*, 2015, **8**, 1707-1711.
11 M. Huang, F. Li, J. Y. Ji, Y. X. Zhang, X. L. Zhao and X. Gao, *CrystEngComm.*, 2014, **16**, 2878-2884.
12 M. Reddy, T. Yu, C.-H. Sow, Z. X. Shen, C. T. Lim, G. S. Rao and B. Chowdari, *Adv. Funct. Mater.*, 2007, **17**, 2792-2799.
13 G. Gao, L. Yu and H. B. Wu, *Small*, 2014, **10**, 1741-1745.
14 M. Zou, J. Li, W. Wen, L. Chen, L. Guan, H. Lai and Z. Huang, *J. Power Sources*, 2014, **270**, 468-474.
15 X. Zhu, Y. Zhu, S. Murali, M. D. Stoller and R. S. Ruoff, *ACS Nano*, 2011, **5**, 3333-3338.
16 X. Liu, W. Si, J. Zhang, X. Sun, J. Deng, S. Baunack, S. Oswald, L. Liu, C. Yan and O. G. Schmidt, *Sci. Rep.*, 2014, **4**, 7452.
17 W. M. Zhang, X. L. Wu, J. S. Hu, Y. G. Guo and L. J. Wan, *Adv. Funct. Mater.*, 2008, **18**, 3941-3946.
18 Z. Zeng, H. Zhao, P. Lv, Z. Zhang, J. Wang and Q. Xia, *J. Power Sources*, 2015, **274**, 1091-1099.
19 G. Zeng, N. Shi, M. Hess, X. Chen, W. Cheng, T. Fan and M. Niederberger, *ACS Nano*, 2015, **9**, 4227-4235.
20 X. Jia, Y. Cheng, Y. Lu and F. Wei, *ACS Nano*, 2014, **8**, 9265-9273.
21 G. Zhou, D.-W. Wang, F. Li, L. Zhang, N. Li, Z.-S. Wu, L. Wen, G. Q. Lu and H.-M. Cheng, *Chem. Mater.*, 2010, **22**, 5306-5313.
22 F. Han, D. Li, W. C. Li, C. Lei, Q. Sun and A. H. Lu, *Adv. Funct. Mater.*, 2013, **23**, 1692-1700.
23 R. Mo, S. O. Tung, Z. Lei, G. Zhao, K. Sun and N. A. Kotov, *ACS Nano*, 2015, **9**, 5009-5017.
24 J. P. Ge, W. Chen, L. P. Liu and Y. D. Li, *Chem. Eur. J.*, 2006, **12**, 6552-6558.
25 F. Bai, D. Wang, Z. Huo, W. Chen, L. Liu, X. Liang, C. Chen, X. Wang, Q. Peng and Y. Li, *Angew. Chem. Int. Ed.*, 2007, **46**, 6650-6653.
26 X. Wang, J. Zhuang, Q. Peng and Y. Li, *Nature*, 2005, **437**, 121-124.
27 X. Liang, X. Wang, J. Zhuang, Y.-t. Chen, D.-s. Wang and Y.-D. Li, *Adv. Funct. Mater.*, 2006, **16**, 1805-1813.
28 J.-P. Jolivet, C. Chanéac and E. Tronc, *Chem. Commun.*, 2004, 481-483.
29 A. C. Ferrari and D. M. Basko, *Nat. Nanotechnol.*, 2013, **8**, 235-246.
30 W. Wei, S. Yang, H. Zhou, I. Lieberwirth, X. Feng and K. Müllen, *Adv. Mater.*, 2013, **25**, 2909-2914.
31 L. Zhao, M. Gao, W. Yue, Y. Jiang, Y. Wang, Y. Ren and F. Hu, *ACS Appl. Mater. Interfaces*, 2015, **7**, 9709-9715.
32 L. Li, A. Kovalchuk, H. Fei, Z. Peng, Y. Li, N. D. Kim, C. Xiang, Y. Yang, G. Ruan and J. M. Tour, *Adv. Energy Mater.*, 2015, 1500171.
33 L. Zhang, H. B. Wu and X. W. Lou, *Adv. Energy Mater.*, 2014, **4**, 1300958.
34 B.-Y. Chang and S.-M. Park, *Annu. Rev. Anal. Chem.*, 2010, **3**, 207-229.
35 Y. Zhang, Q. Zhuo, X. Lv, Y. Ma, J. Zhong and X. Sun, *Electrochim. Acta*, 2015, **178**, 590-596.
36 C. Hu, L. Lv, J. Xue, M. Ye, L. Wang and L. Qu, *Chem. Mater.*, 2015, **27**, 5253-5260.
37 S. Y. Jeong, S. Yang, S. Jeong, I. J. Kim, H. J. Jeong, J. T. Han, K. J. Baeg and G. W. Lee, *Small*, 2015, **11**, 2774-2781.
38 J. Wang, H. Zhou, J. Nanda and P. V. Braun, *Chem. Mater.*, 2015, **27**, 2803-2811.
39 X. Huang, H. Yu, J. Chen, Z. Lu, R. Yazami and H. H. Hng, *Adv. Mater.*, 2014, **26**, 1296-1303.
40 X. Leng, S. Wei, Z. Jiang, J. Lian, G. Wang and Q. Jiang, *Sci. Rep.*, 2015, **5**, 16629.
41 J. Wang, C. Zhang and F. Kang, *ACS Appl. Mater. Interfaces*, 2015, **7**, 9185-9194.
42 S. Bai, S. Chen, X. Shen, G. Zhu and G. Wang, *RSC Adv.*, 2012, **2**, 10977-10984.

Graphical Abstract